Progress in Neurobiology 205 (2021) 102116

Contents lists available at ScienceDirect

Progress in Neurobiology

journal homepage: www.elsevier.com/locate/pneurobio

Original Research Article

Motor-like neural dynamics in two parietal areas during arm reaching

S. Diomedi [a,1], F.E. Vaccari [a,1], C. Galletti [a], K. Hadjidimitrakis [a,b,*], P. Fattori [a,b,*]

[a] Dept. of Biomedical and Neuromotor Sciences, University of Bologna, Italy
[b] Alma Mater Research Institute for Human-Centered Artificial Intelligence, University of Bologna, Italy

ARTICLE INFO

Keywords:
Motor control
Parietal cortex
Hidden Markov Model
Neural states
Sensorimotor

ABSTRACT

The classical view on motor control makes a clear distinction between the role of motor cortex in controlling muscles and parietal cortex in processing movement plans and goals. However, the strong parieto-frontal connections argue against such clear-cut separation of function. Modern dynamical approaches revealed that population activity in motor cortex can be captured by a limited number of patterns, called neural states that are preserved across diverse motor behaviors. Whether such dynamics are also present in parietal cortex is unclear. Here, we studied neural dynamics in the primate parietal cortex during arm movements and found three main states temporally coupled to the planning, execution and target holding epochs. Strikingly, as reported recently in motor cortex, execution was subdivided into distinct, arm acceleration- and deceleration-related, states. These results suggest that dynamics across parieto-frontal areas are highly consistent and hint that parietal population activity largely reflects timing constraints while motor actions unfold.

1. Introduction

Like other primates, arm movements to reach and grasp objects are fundamental in our daily lives and are mainly driven by vision. Visual information enters the cortex at the level of the occipital lobe and proceeds rostrally via the posterior parietal cortex (PPC) to the motor areas of the frontal cortex to generate a motor response. The motor cortex has been reported to process either low-level signals such as muscle forces (Ben Hamed et al., 2007) or torques (Scott and Kalaska, 1997) and high-level movement kinematics (Georgopoulos et al., 1982), with its precise role in movement generation still under debate (Omrani et al., 2017). Recent advances in understanding motor processing were made by studies that focused on the activity of large populations of neurons in motor cortex (Gao and Ganguli, 2015; Luczak et al., 2015; Sadtler et al., 2014; Shenoy et al., 2013). Differently to classic representational approaches, based on correlations between single cell activity and movement features, modern approaches consider the whole neuronal population as a 'dynamical system', i.e., an internal generator of optimized activity patterns that trigger motor behavior (Michaels et al., 2016; Omrani et al., 2017; Shenoy et al., 2013). The dynamical system approach discovered low-dimensional dynamics in motor and premotor cortex population activity with important rhythmic and rotational components also in non-rhythmic movements such as reaching or grasping (Churchland et al., 2012; Gallego et al., 2018; Shenoy et al., 2013; but see also Suresh et al., 2020). In this view, rotations seem to be a simple element of the dynamic oscillatory patterns required to produce muscle contractions and relaxations (Shenoy et al., 2013).

It is commonly accepted that the PPC is the major cortical site of multisensory integration for limb movement guidance and single PPC neurons show highly heterogeneous responses (Andersen et al., 2014; Buneo and Andersen, 2006; Diomedi et al., 2020; Fattori et al., 2017; Hadjidimitrakis et al., 2019; Janssen and Scherberger, 2015; Medendorp and Heed, 2019; Zhang et al., 2017). Given the extensive bi-directional connections within the fronto-parietal network (Gamberini et al., 2020; Johnson et al., 1996; Matelli et al., 1998), we examined whether population activity in parietal cortex mostly reflected both the temporal dynamics and the low-dimensionality of the population activity variance observed in frontal areas. We studied neural populations in two medial PPC areas, namely V6A and PEc, during a reaching task in 3D space. Both areas process visual and somatosensory information (Gamberini et al., 2011, 2018) and neural activity is modulated by eye position and arm movement related signals (Breveglieri et al., 2012; Fattori et al., 2001; Galletti et al., 1995; Raffi et al., 2008;). To study population dynamics, we applied the Hidden Markov Model (HMM), an unsupervised machine learning method used for time series analysis (Rabiner, 1989). The HMMs identify, within the time-evolving population activity,

* Corresponding authors at: Dept. of Biomedical and Neuromotor Sciences, University of Bologna, Italy.
E-mail addresses: kon.chatzidimitrakis@unibo.it (K. Hadjidimitrakis), patrizia.fattori@unibo.it (P. Fattori).
[1] Authors that contributed equally to the work.

https://doi.org/10.1016/j.pneurobio.2021.102116
Received 5 March 2021; Received in revised form 18 May 2021; Accepted 29 June 2021
Available online 2 July 2021

discrete 'neural hidden states' through the observed noisy discharges. In premotor cortex, HMMs detected different states of population activity, reflecting baseline activity and arm movement planning discharges (Kemere et al., 2008). A recent study characterized distinct sub-populations in premotor and motor areas applying HMM (Mazurek et al., 2018). Additionally, in motor cortex, the decomposition of arm movement into two different neural states, corresponding to acceleration and deceleration phases, was reported using HMM (Kadmon Harpaz et al., 2019).

In parietal areas V6A and PEc, we reliably detected a number of neural states that were tightly linked to distinct periods of the task sequence, i.e. the planning and execution phases of movement and the holding of target. The states before and after the movement could be further segmented into two states related to different stages of movement planning and arm posture processing. Rather unexpectedly, we found that activity during the movement could be parsed into two states of equal duration temporally linked to the acceleration and deceleration phases, exactly as observed in motor cortex with a different reaching task (Kadmon Harpaz et al., 2019). Our findings suggest that, at least during arm reaching in 3D space under static sensory input, PPC cortex shows low-level population neural dynamics. In addition, the present findings suggest that computational processes in PPC could be better understood if studied using a dynamical system approach rather than a mosaic of single independent units, as already proposed for the motor cortices (Churchland et al., 2012; Shenoy et al., 2013).

2. Materials and methods

The current study consisted in an extended computational analysis of neural data reported previously (Hadjidimitrakis et al., 2014, 2015). Accordingly, the procedures described herein focus on analytical treatment of the data and provide only essential details of the experimental procedures. Full details of experimental methods are provided in our previous reports.

The study was performed in accordance with the guidelines of the EU Directives (86/609/EEC; 2010/63/EU) and the Italian national law (D. L. 116−92, D.L. 26–2014) on the use of animals in scientific research. Protocols were approved by the Animal-Welfare Body of the University of Bologna. During training and recording sessions, particular attention was paid to any behavioural and clinical sign of pain or distress.

2.1. Experimental procedures

Two male macaque monkeys (Macaca fascicularis) weighting 4.4 kg (M1) and 3.8 kg (M2) were used. Single cell activity was extracellularly recorded from the anterior bank of the parieto-occipital sulcus (POs) and the adjacent caudal part of SPL.

Multiple electrode penetrations were performed using a five-channel multielectrode recording system (Thomas Recording GmbH, Giessen, Germany). The electrode signals were amplified (at a gain of 10,000) and filtered (bandpass between 0.5 and 5 kHz). Action potentials in each channel were isolated with a waveform discriminator (Multi Spike Detector; Alpha Omega Engineering Nazareth, Israel) and were sampled at 100 kHz. The quality of single-unit isolation was determined by the visual inspection of spike wave forms and considering refractory periods in ISI histograms during spike-sorting. Only well-isolated units with homogenous waveforms and clear ISI histogram were considered. The animal behaviour was controlled by custom-made software implemented in Labview (National Instruments, Austin, TX) environment (Kutz et al., 2005). Eye position signals were sampled with two cameras (one for each eye) of an infrared oculometer system (ISCAN, Woburn, MA) at 100 Hz. The vergence angle was not recorded online, but it was reconstructed offline from the horizontal eye positions of the two eyes. A sort of control for vergence resulted from the presence of electronic windows (one for each eye, $4^\circ \times 4^\circ$ each) that controlled the fronto-parallel gaze position, so that we could set an offset of the horizontal eye position signal for targets located in the same direction, but at different depths.

Histological reconstruction of electrode penetrations was performed following the procedures detailed in studies from our lab (Gamberini et al., 2011, 2018). Briefly, electrode tracks and location of each recording site were reconstructed on Nissl-stained sections of the brain on the basis of several cues: 1) marking electrolytic lesions, 2) the coordinates of penetrations within the recording chamber, 3) whether the electrode passed through another cortical area before reaching the region of interest. Area V6A was initially recognized on functional grounds following the criteria described in Galletti et al. (1999) and later confirmed based on the cytoarchitectonic criteria reported in Luppino et al. (2005). The recording sites were assigned to area PEc according to the cytoarchitectonic criteria of Pandya and Seltzer (1982) and Luppino et al. (2005).

2.2. Behavioural task

Electrophysiological signals were collected while the monkeys performed an instructed-delay foveated reaching task (Fig. 1c), towards targets that were located at different positions in the 3D space. Monkeys sat in a primate chair, with the head restrained, and faced a horizontal panel located at eye level. Nine light-emitting diodes (LEDs) mounted on the panel at different directions and distances from the eyes were used as both fixation and reaching targets (Fig. 1b, left). As shown in the right part of Fig. 1b, the LEDs were arranged in three rows: one central, along the sagittal midline, and two laterals, at version angles of -15° and $+15^\circ$, respectively. Along each row, three LEDs were located at vergence angles equal to 17.1°, 11.4°, and 6.9°, respectively. The two animals had the same interocular distance (3.0 cm), so the targets in each row were placed at the same distance from the monkeys' mid-eye level in both animals (nearest/intermediate/far targets: 10/15/25 cm, respectively). The range of vergence angles was chosen to be within the limits of peripersonal space, so the monkeys were able to reach all target positions. The animals performed the task with the limb contralateral to the recording site while maintaining steady fixation. The hand started the trial pushing a button (home button, HB, 2.5 cm in diameter, Fig. 1b) placed outside the monkeys' visual field, 5 cm in front of its trunk. After 1 s, one of the nine LEDs lit up green and the monkeys were required to fixate it while keeping the button pressed. The monkeys had to withhold any eye or arm movement for 1700–2500 ms, until the 'go' signal that was the change of LED colour (green to red). After the 'go' signal the animal had 1 s to release the HB (movement onset) and start an arm movement to reach the target. Target touch was acquired as the activation of a micro-switch positioned at LED basis (movement end). After reaching the target LED the monkeys had to hold it for 800–1200 msec. Then, the LED offset cued the monkeys to release it and move their arm backward to press the HB in order to receive reward. Only rewarded trials were used in further analyses.

2.3. Hidden Markov Model

We used the Hidden Markov Model (HMM) method to examine whether the PPC activity could be characterized by sequences of discrete and stable patterns of activity termed hidden states. The HMM assumption is that a sequence of observable symbols is generated by a sequence of underlying hidden, not directly observable states (Fig. 1d). The hidden state sequence is a Markov chain (or process) since the future state of the system stochastically depends only on the present state and not on the past.

In general, an HMM is characterized by different parameters:

1 the number (N) of hidden states in the model. We defined $S = \{S_1, S_2, \ldots, S_N\}$ the set of possible states and q_t the Markov process that represents the state of the system at time t. The Markov process

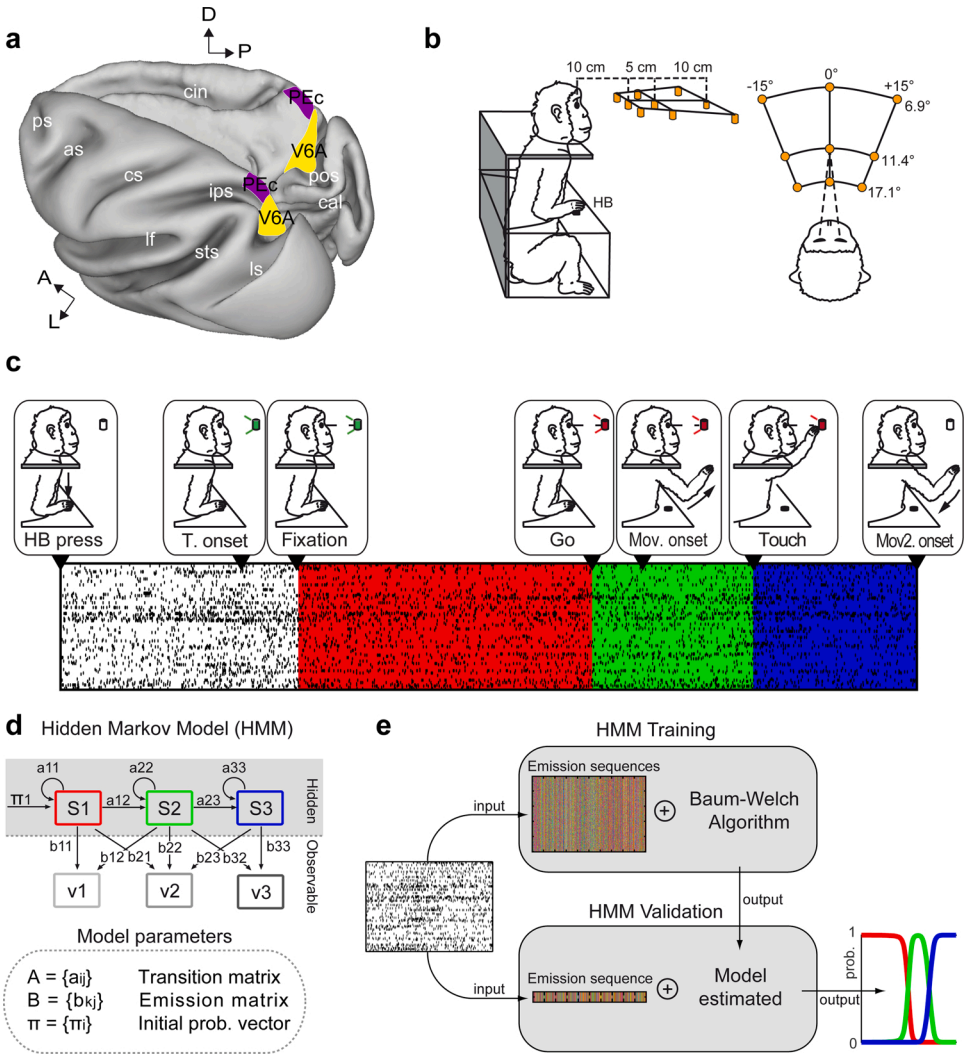

Fig. 1. Anatomical localization of V6A and PEc, experimental design and Hidden Markov model. a) 3D reconstruction of macaque brain. Dorsal view of the left hemisphere and medial view of the right hemisphere showing area V6A (yellow) and PEc (purple). Abbreviations: as, arcuate sulcus; cal, calcarine sulcus; cs, central sulcus; cin, cingulate sulcus; ips, intraparietal sulcus; lf, lateral fissure; ls, lunate sulcus; pos, parieto-occipital sulcus; ps, principal sulcus; sts, superior temporal sulcus; D, dorsal; P, posterior; A, anterior; L, lateral. b) Experimental setup. Reach movements were performed in darkness toward 1 of 9 LEDs arranged at eye level in front of the monkey. Spatial coordinates of targets are indicated as vergence and version angles of the eyes. HB: Home Button. c) Task sequence. From left to right: trial start (HB press), target appearance (T. onset), fixation onset (Fixation), go signal (Go), start of the arm movement (Mov. onset), touch and holding of the target (Touch), return movement (Mov2. onset). The rasters reported below are an example of neural activity pooled together to simulate an ensemble. d) Schematic representation of the HMM and its core parameters. The Markov process starts with initial probabilities π to be in one of the N states (maximum probability is assigned to the first state) and it proceeds though a series of state transitions with a probability determined by the Transition Matrix (A). The Markov process itself is not observable (hidden), but the Emission Matrix (B) links in terms of probability this process to a series of observable events [v_1, v_2, v_3 …] that indicate in which hidden state is the system. e) HMM training and validation on neural data. Spike counts are converted in emission sequences. During the training phase, the Baum-Welch algorithm estimates the model parameters (transition and emission matrices). These are validated on new emission sequences to give a state probability sequence (HMM validation, see Methods).

assumes the probability of transition from state S_i to S_j at time t + 1 depends only on the state of the system at time t:

$$P(q_{t+1} = S_j | q_t = S_i, q_{t-1} = S_k, \ldots) = P(q_{t+1} = S_j | q_t = S_i)$$

2 the number (M) of distinct observable symbols i.e. the alphabet size. We denote symbols as $V = \{v_1, v_2, \ldots, v_M\}$. A so-called emission sequence is formed by symbols in V and it represents the experimental observations. We will use these emission sequences to train and validate the model.

3 According to the Markov Process, the probability to switch from a hidden state to another (state transition) is given by the transition matrix $A = \{a_{ij}\}$ where:

$$a_{ij} = P(q_{t+1} = S_j | q_t = S_i) 1 \quad \leq \quad i,j \quad \leq \quad N$$

Noteworthy, this matrix tells which status steps are allowed and which not, so it defines the topology of the Markov Process itself. Indeed, if the system can go from any state to another, we will have $a_{ij} > 0 \ \forall i.j$. If any state transitions are not allowed, we will have the relative element $a_{ij} = 0$.

4 The emission matrix $B = \{b_{hj}\}$ links the hidden state sequence (i.e. the Hidden Markov Process) to the observable emission sequence. In brief, it represents the probability to observe the h[th] symbol during the j[th] state and so:

$$b_{hj} = P(v_h \quad at \quad t | q_t = S_j)$$

For neural data, the emission matrix represents the probability to observe a spike from the h[th] neuron during the j[th] state.

5 The vector initial probability $\pi = \{\pi_i\}$ indicates the initial probability for each HMM state at the first observation:

$$\pi_i = P(q_1 = S_i) \quad 1 \quad \leq \quad i \quad \leq \quad N$$

The initial probability is required to initiate the Markov Process.

A Hidden Markov Model is identified by these three parameters (A, B, π).

2.3.1. *HMM training and decoding of hidden states probability*

We use the Baum-Welch algorithm to train the models and so to estimate its main parameters, i.e. the transition and the emission matrix (Fig. 1e). This algorithm is an iterative procedure, based on the Expectation Maximization algorithm, that starting from an initial model defined by choosing randomly initial parameters, it iteratively generates a new model upgrading the initial parameters and maximizing the probability that the new model has generated the experimental observations used. The algorithm ends either after 500 iterations or when the

difference between the log-likelihood of the model at kth step and that of the (k-1)th is less than 10^{-6}. Given a trained model and an entire experimental observation $n_{1:T}$ of length T (i.e. the total number of bins) we wanted to decode $P(q_t = S_j|n_{1:T})$, i.e. the probability at each time instant to be in one of the defined hidden states (Fig. 1e). For this aim we used the Forward Backward algorithm. This method uses the forward density representing information from the beginning forward to the present t:

$$\alpha_t(j) \equiv P(n_{1:t}, q_t = S_j) = \left[\sum_{i=1}^{N} \alpha_{t-1}(i) a_{ij}\right] b_{n_t j}$$

and the backward density that represent the information from time T backward to the present t:

$$\beta_t(j) \equiv P(n_{t+1:T}, q_t = S_j) = \sum_{i=1}^{N} \beta_{t+1}(i) a_{ji} b_{n_{t+1} i}$$

to infer the a posteriori likelihood (APL) that is proportional to the probability we wanted to decode (Kemere et al., 2008):

$$P(q_t = S_j|n_{1:T}) \propto P(n_{1:T}, q_t = S_j) = \alpha_t(j)\beta_t(j)$$

2.3.2. Neural implementation of HMM

In our HMM implementation, we used a single observation variable approach for simplicity and in accordance with previous works (Bollimunta et al., 2012; Mazurek et al., 2018; Mazurek and Schieber, 2019). We performed a random selection procedure during data pre-processing (see below) to account for multiple observations and avoid information loss. In particular, N was the number of the neural states that we expected to be encoded in the population activity. Our alphabet was composed by the numbers from 1 to the total number of neurons in the population plus 0 that represented the absence of spikes from any neuron. The resulting alphabet size M is equal to number of units in our population plus one. To feed the HMM algorithm, we needed to generate the appropriate emission sequences from the neural data. Starting from a spike count for each cell and each trial (2-ms bins) aligned all at the same event, in order to generate an emission sequence, we assigned one symbol to each bin (Bollimunta et al., 2012; Mazurek et al., 2018). For example, we assigned the symbol "2" to a bin in which we recorded a spike from the 2-nd neuron of our population. If no cell discharged at a particular bin, we put the symbol "0". If two or more neurons discharged in the same bin, we chose one of them in a random way. On average, in a trial we had 11 % of the total bins with no spikes, 23 % with only spike from 1 neuron and 66 % with spikes from 2 or more neurons. Forcing these discharges in a unique emission sequence representative of the trial would create a bias due to the randomness of the choice and it would lead to a loss of information of about 42 % (considering the number of spikes occurred simultaneously that would not be considered over the total). To avoid bias and the information loss, we 'augmented' the initial data by repeating 100 times/trial the procedure, thus obtaining 100 emission sequences/trial that were slightly different one from another (1000 seq. for each target position tested on 10 trials). This procedure, that could be seen as performing a kind of 'bootstrapping' within the population of neurons active in each bin, enabled us to obtain a number of emission sequences that fully represented the original data (99.98 % of probability to observe the entire information with 100 seq./trial vs $\simeq$ 85 % with 50 seq./trial; simulated data). For each neural population (M1, V6A and PEc; M2, V6A and PEc), we trained an HMM separately for each target position. Because the Baum-Welch maximization is sensitive to the initial values used, during the train step, we ran the algorithm 10 times for every position and population starting each time with different initial parameters and we selected the model with the highest log-likelihood (Mazurek et al., 2018). The elements of the emission matrix were initialized as equal to *1/M*. The diagonal elements of transition matrix (i.e. the probability to remain in a state) were initialized with values in the range $a_{i,i} \in [0.99,0.999]$, and elements above the diagonal (i.e. the probability to proceed to the next state) were set as $a_{i,j} = (1 - a_{i,i})/(1 - N)\ \forall\ j > i$ where *N* is the total number of the states. We then normalized the rows of the matrix to obtain a total probability equal to 1.

To avoid over fitting, the models were cross validated in two different ways. For the preliminary consistency analysis (i.e. to choose the optimal number of states), we trained the models on emission sequences generated from all the available trials and we decoded sequences generated in the same way but with an additional bins shuffling step (i.e. the tth-bin of the jth-sequence was randomly substitute with tth-bin of the ith-sequence). This atypical cross-validation allowed to test the models on data not completely new, but not identical to the training dataset, with a great computational advance. For all the subsequent analyses, we used a leave-one-out cross-validation (models trained on 9 trials and validated on the 1 left out) and all the subsequent results here reported are referred to the validation dataset, never seen by the models.

2.4. Consistency and timing analysis

Given a trained N-state model ([N x N] transition matrix; [n° of neurons x N] emission matrix), we considered 'consistent' with the model every emission sequence in which the probabilities of N-states crossed a threshold. We arbitrarily chose the threshold to be equal to 0.7, a slightly higher value compared to similar works (e.g., 0.6 in Mazurek et al., 2018). For the timing analysis, we took the first bin in which a state rose above the threshold ('rise' of the state) or the last bin before it fell under the threshold ('fall' of the state) considering only sequences that were consistent with the model of interest. To compare V6A and PEc areas, we performed a series of Wilcoxon test ($p < 0.05$, data from M1 and M2 pooled together) for each state rise and fall. We calculated the variability in the timing of the 'real' neural transitions adjusted for the timing variability of the behavioral events. To do so, we subtracted the variance of the reference event timing from the variance of the decoded neural transition timing.

2.5. Gini coefficient

The Gini coefficient (or index) was used to measure the sparsity of a matrix. We computed the Gini index of the emission matrices to investigate which fraction of the population was active during each hidden state. Thus, in our case, a highly sparse emission matrix (high Gini coefficient) indicated that in each hidden state only few neurons were likely to discharge. Vice versa, we expected a low Gini coefficient when each state involved the activation of the majority of the population (low sparsity of the emission matrix). To have reference values, we generated 3 blocks of synthetic [100 neurons x 3 states] emission matrices (10,000 each block). The first block contained matrices with only a random element between 0 and 1 for each row simulating a population of neurons with variable activity in one hidden state (i.e. highly selective). All the other elements of the matrices were set to 0. The second block contained matrices with two random elements per row in the range [0,1] and the other set to 0, while the third block contained matrices with all the elements different from 0. Probabilistically, these 3 blocks of synthetic emission matrices simulated 3 different neural populations with the 1/3 (33.3 %), 2/3 (66.7 %) and 3/3 (100 %) of the units active during each state. We computed the Gini coefficient on all the matrices to obtain 3 reference distributions of synthetic values.

2.6. Comparisons between state sequences

To compare two different state sequences decoded by the HMM algorithm and characterized by T bins and N states, we obtained two numeric vectors with N x T elements concatenating the probability of the N states for each sequence. We then computed the R^2 between the two vectors as a measure of their similarity (values near 1 meaning that the two curves perfectly match).

Based on this measure, we developed a procedure to test if the two

sequences of interest were significantly different or not. Starting from the trained models (real models) that had produced the state sequences of interest (real state sequences), we generated 200 new state sequences (100 fake state sequences for each model to compare) shuffling the emission matrices of the real models along the columns (states). Note that by shuffling training models we obtained biologically plausible fake models (i.e. with plausible probabilities to observe spikes from the cells) assigning to one neuron the probability to discharge in the same state of a different neuron (randomly chosen without repetition). We then computed a Gaussian null distribution calculating the R^2 between each of the real state sequences and the fake sequences. The null distribution represented the reference values of the R^2 for different sequences (real vs randomly generated). We considered the two real sequences as not significantly different if their R^2 was higher than the null distribution (Z-test, $p < 0.05$).

2.7. Sliding window t-test

To examine whether the results obtained with the HMM were present also at single cells, we performed a sliding window *t*-test analysis. We repeated the same procedure within different temporal intervals. Basically, we used the same temporal intervals of interest where we had applied HMM and we took a fix time window as reference. This fixed time window coincided with one of the average hidden states detected, thus its time width depended on the mean duration of the state. For each cell, we then performed a series of *t*-tests ($p < 0.05$) between the firing rate computed in the fixed time window and the firing rate computed in a sliding window of equal width that moved in 10-ms steps. For each step, we calculated the percentage of the cells in the population that showed a significant change in firing rate with respect to the fixed window (mean and standard deviation of 5000 bootstrap samples). As a control, we repeated the procedure taking as reference an initial and a final 300 ms window that extended from −1000 to −700 and from +700 to +1000 ms with respect to movement onset, respectively (Fig. S5).

2.8. Neural trajectories

We projected the high-dimensional data on a reduced 3D-space using a standard Principal Component Analysis (PCA). We analysed recordings starting 1000 ms before movement onset and ending 1000 ms after. Since neural data were not recorded simultaneously, we aligned the data across different trials assigning a fixed number of bins to each of the main behavioural epochs (Delay, 370 bins; Reaction time, 130 bins; Movement, 190 bins; Hold, 310 bins) such that the total number of bins was 1000 and the average bin width was ≈2ms. We then smoothed (Gaussian filter, sigma ≈ 110 ms) the binned spike trains for each trial separately and computed the condition averages. With these data, we built a [m x n] matrix where m = N° of cells and n = N° bins * N° conditions; we normalized in the range [0,1] along the rows to avoid high firing rate units to excessively influence the analysis and we then performed the PCA on the pooled neural data.

To investigate the temporal evolution of population activity within each hidden state, we fragmented the 3D - neural trajectories averaged across trials of the same condition in 6 segments, one for each hidden state (DELAY, PREMOV, ACC, DEC, EARLY HOLD, HOLD) obtaining 54 segments in total (6 states * 9 conditions). Each segment was resampled at 20 equally spaced points and the centroid of each segment was aligned with the origin of the axes. We computed the mean Euclidean Distance between all the points (20) of segments belonging to the same state (intra-state distance) or belonging to different states (inter-state distance): lower distances meant similar segments shapes (i.e., similar temporal evolution of the neural trajectory segments).

3. Results

Our dataset consisted of neurons recorded from two areas, namely V6A, located in the anterior bank of parieto-occipital sulcus and PEc, in the adjacent caudal sector of medial PPC (Fig. 1a). Data were collected from two monkeys (M1 and M2) trained to perform an instructed delay reaching task towards visual targets (light emitting diodes, LEDs) located in 9 different positions (3 directions x 3 depths), placed at eye level (Fig. 1b). The animal sat on a primate chair in complete darkness and pressed a home button (HB) to begin the trial. Randomly, one of the LEDs was switched on and monkey had to fixate its gaze on it. After a variable delay, the LED changed colour and this cued the animal to perform an arm reaching movement and hold the reached position. After a variable period, the LED turned off and the animal moved its arm back to the HB position to receive reward (Fig. 1c). Movement onset was defined by the release of the HB, as detected by the embedded microswitch (1 ms resolution). Movement end was measured as activation of a microswitch positioned on the target.

Cells with activity recorded for 10 correct trials for each target were used for analysis, without any further preselection. Data from different recording sessions were pooled together to construct four neural ensembles (2 animals x 2 areas) that were analyzed with population methods. Neural ensembles consisted of 104 and 93 units from V6A and PEc, respectively in monkey M1; 105 and 83 neurons respectively, from V6A and PEc in monkey M2 (see Fig. S1a for the recording sites).

Fig. 1d shows a simple scheme of an HMM. In this view, a neural population goes through a chain of hidden states that makes each unit discharging with different probabilities. The transition matrix contains the probability to switch from each state to another, defining the topology of the Markov process. The emission matrix in turn, estimates the probability to observe a spike from each neuron in each state and it represents the link between the recorded neural activity and the unobservable sequence of hidden states. Like any machine learning method, an HMM involves a training step to estimate the optimal parameters of the model i.e. the transition and the emission matrices and the subsequent decoding on a test data set (Fig. 1e). Then, given an observed spike train, we used the estimated model to infer the probability at each time instant to be in one of the possible states (i.e. the state probability sequence or state sequence, Fig. 1e). We converted the spike counts in emission sequences and we cross-validated every model to ensure the predictive capacity of our model (see Methods).

3.1. 'Macro' neural states corresponded to main task phases

A crucial problem in HMMs is the definition of the optimal number of hidden states that represent the different patterns of activity. We addressed this issue with two different approaches while analyzing a time interval spanning from 1000 ms before the arm movement start until 1000 ms after to include the main behavioral events of the task.

First, we checked the consistency of different numbers of states. For this analysis, we trained HMMs with different numbers of states (from 2 to 7), then we used the trained models to decode each testing sequence, obtaining each time a different state probability sequence. A state sequence decoded by a *N*-states model was defined 'consistent' if the algorithm detected *N* hidden states with a probability above the threshold. Optimal was the number of states that decoded the highest percentage of consistent sequences in the testing dataset (see Methods).

Fig. 2a shows the percentage of the emission sequences in which 2, 3, 4, 5, 6 or 7 neural states were consistently decoded. In both areas, 2 and 3 states were detected in the 100 % of the emission sequences in both animals; 4 states were present in about the 60 % of the sequences (M1: 59 % and 68 % in V6A and PEc, respectively; M2: 42 % and 69 %). Adding more states, the percentage of consistency further decreased. According to the percentage of consistent decoded sequences, both 2 and 3 (scoring a consistency of 100 %) could be considered as the optimal number of states.

The second approach was to compare the goodness of fit (estimated as log-likelihood) of the models trained previously (Fig. S1b). The HMM with the optimal number of states should have the highest log-

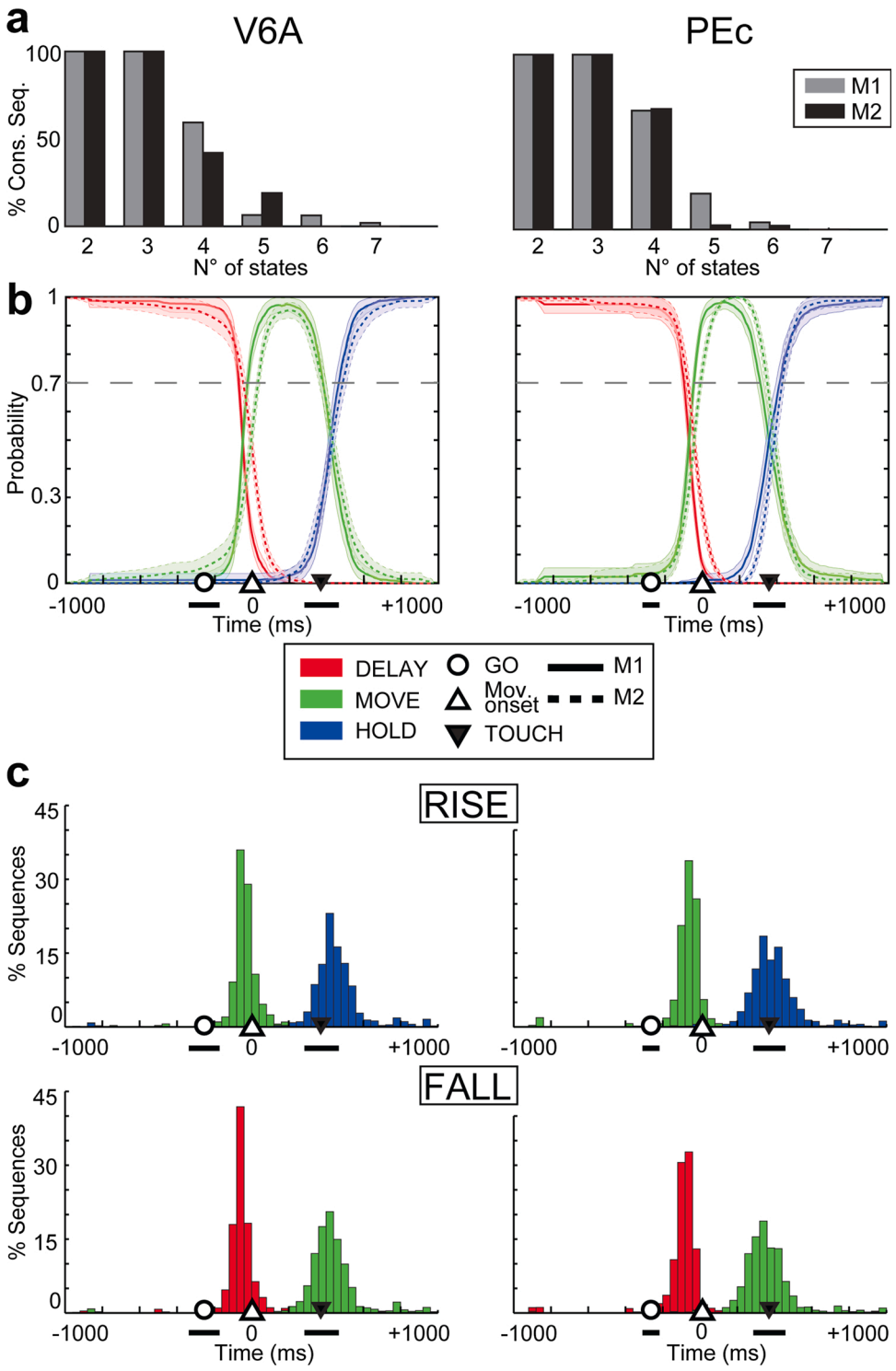

Fig. 2. Consistency analysis and results for 3-state HMM. a) Bars indicate the percentage of sequences in which it was possible to find a different number of neural states (2-7). We found that 3 was the highest number of states detectable in almost all the sequences. b) Average state sequences for 3-state HMMs. Colored lines (continue for M1, dashed for M2) represent the time course of the probability of each state. Shaded areas: ± S.E.M. across trials.. Symbols: timing of main behavioral events averaged across trial and positions. Black thick lines under symbols: variability of event timing (mean ± S.D). Horizontal dashed line: threshold set to identify 'active' states (0.7). The model individuated 3 different neural states along the trial highly consistent across animals and areas. c) Timing of state rises (i.e., when its probability exceeded the threshold) or falls (when vice versa its probability fell above the threshold). Y-axis: the frequency expressed as percentage of emission sequences. Every column of the histogram has a temporal resolution of 40 ms (20 bins). Symbols: timing of main behavioral events averaged across trial and positions. Black thick lines under symbols: variability of event timing (mean ± S.D). The distributions of rises / falls indicate that the switches between one neural state and another were tightly related to main behavioral events.

likelihood. In agreement with the consistency analysis, the models with 2 and 3 states had the highest log-likelihoods. In addition, after visual inspection of the data it was evident that the states decoded by 2-state models could result from 3-state models by merging two adjacent states (the first with the second or the second with the third, depending on the sequence; see Fig. S1c). Given this, we chose 3 -instead of 2- as the optimal number of hidden states for the subsequent analyses.

Fig. 2b shows the average state probability sequence of 3-state HMMs trained separately for each target position. Comparing across areas (Fig. 2b, left and right panels) and animals (Fig. 2b continuous and dashed line), showed that the probabilities and timing of the activity patterns were quite similar. An initial state was present from the start of the analysis window (red lines) and its probability sharply decreased about 50 ms before arm movement onset. Around this time, a second state (green line) emerged and was present for ~0.5 s, until the end of movement. After that, a third state (blue line) rose and lasted until the end of the analysis window. The thin shaded areas shown in the figure indicated a high consistency across trials of the state sequence probability (see also below the little variability of state transition timing). To measure the similarity of the state probability sequences across animals

and areas, we computed the R^2 between them. The R^2 values were compared against a null distribution of synthetic shuffled data (see Methods). The state sequences were not statistically different in all the possible comparisons with R^2 values higher than 0.95 (see Table S1). The timing of these three states coincided with the main task epochs i.e. waiting for the 'go' signal, moving the arm towards the target LED and holding the target. Accordingly, we named these 3 hidden states after the main task epochs as DELAY, MOVE and HOLD.

To evaluate in finer resolution the timing of transitions between the three hidden states and compare it across animals and cortical areas, we applied a threshold (0.7, black dashed line in Fig. 2b). Each transition included the 'fall' of one state (probability<0.7 threshold) and the 'rise' of the subsequent state (probability> = 0.7). Fig. 2c shows the rise and fall distributions, separately for each area (pooling together data from the two animals). In all transitions, the distributions of 'fall' of one state and 'rise' of the subsequent overlapped extensively. Importantly, the distribution peaks fell remarkably close to the behavioral events. In V6A and PEc the state DELAY ended at −60 ± 146 (mean ± S.D.) and −89 ± 129 ms, respectively relative to movement onset, whereas the state MOVE rose in V6A and PEc at −28 ± 142 ms and −59 ± 130 ms, respectively, always in relation to the same event. With regards to the movement end, the state MOVE fell in V6A and PEc at 45 ± 145 ms and 0 ± 125 ms, respectively, whereas the state HOLD rose at 78 ± 145 ms and 32 ± 124 ms, respectively for V6A and PEc. Comparing the 2 areas, we observed statistically significant differences in timing, with PEc leading V6A by 38 ms on average (Wilcoxon test, $p < 0.05$, see Methods). Moreover, since the timing of the behavioral events could vary on a trial-by-trial basis, correcting for this variability further reduced the variability of the state transitions to a range equal to ± 33−62 ms.

3.2. Emission matrices reveal the sustained response of neurons over multiple neural states

For each state and neuron, the model estimated a value between 0 and 1 that quantifies the probability to observe a spike from that neuron during a given state and this information was collected in the emission matrix. Fig. 3a illustrates the emission matrix averaged across targets, with rows corresponding to the various states and columns representing neurons, with the color intensity being proportional to their activity. Neurons were sorted in descending order of state selectivity measured as the variance of the emission probability vector.

To test whether the hidden states relied only on the neurons with high state selectivity (high variance) or, conversely, on the entire population, we trained an additional set of HMMs excluding from the population 10 % of the most state selective neurons (the units on the left of the matrices shown in Fig. 3a, see Methods). The state sequences decoded by these 'reduced' HMMs (Fig. S2) were very similar to the ones decoded by the 'complete' HMMs (Fig. 2b), suggesting that the different activity patterns included the whole population and not only the cells tuned selectively for certain states. Indeed, the R^2 between the 'reduced' and the 'complete' state sequences resulted to be very highly correlated (see Table S2 in the Supplementary Material).

We further investigated the relation between neural states and single unit activation by computing the Gini coefficient on the emission matrix (Maboudi et al., 2018). The Gini index ranges between 0 and 1 and measures the sparsity of a matrix. A high Gini index (≃1) indicates that neural states strongly activate a few units. Conversely, a low Gini index (≃0) shows that the entire population is active in each neural state. Fig. 3b shows the median Gini index in the 4 neural populations and the median Gini index value of synthetic populations composed of cells with high, medium and low state selectivity (see Methods). The Gini values

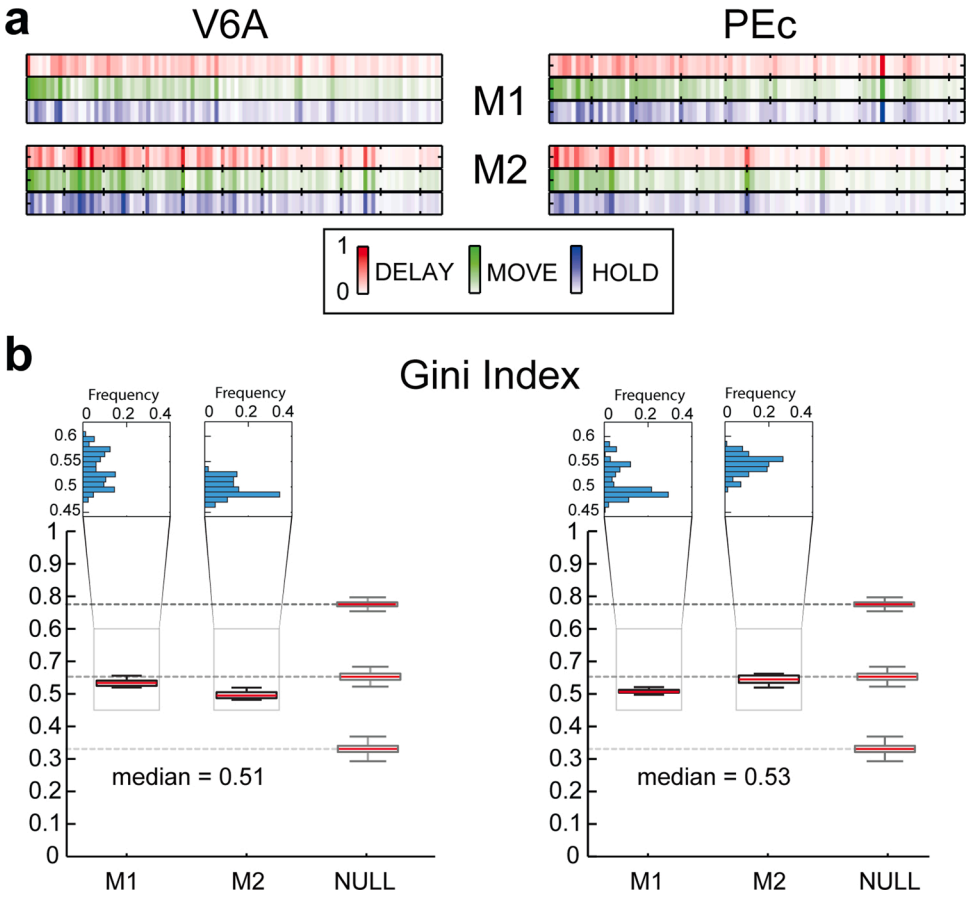

Fig. 3. Single cell contribution to the neural states. a) Graphical representation of the emission matrices averaged across positions. Cells (columns) are sorted in descending order (left to right) based on the variance of the probability to fire a spike in each state. The cells selective for one/two states are shown on the left part of each matrix and nonselective cells are shown on the right part. b) Gini Index calculated on the emission matrices for V6A (left) and PEc (right). The index computed on the real data is compared with the index computed on synthetic data (NULL). In each boxplot, the median and the 25th and 75th percentiles, respectively, are shown. The whiskers extend to the most extreme data points not considered outliers. All the 4 populations have Gini Index not different from that of a synthetic population in which, during each neural state, 2/3 of the cells are active. The inserts at the top show in detail the distributions of the Gini indexes computed on the real data.

for the real data were very similar to a synthetic population with a median Gini index equal to 0.55 constructed with the assumption that the 66 % (2/3) of cells were active during each state.

3.3. HMMs in restricted time windows revealed several 'micro' states

For simplicity, we will refer to the 3 neural states before mentioned as 'macro' states because they were detectable in all the analyzed emission sequences considering a large temporal window (2000 ms, centered on movement onset). Our analyses so far were based on the 3-state model; however, 4-state models also provided a high consistency of decoding (Fig. 2a). In 4-state models, the 3 'macro' states described previously were still detected and in addition a fourth state popped up either between DELAY and MOVE, or between MOVE and HOLD states (Fig. S3). To investigate these additional states, we analyzed the timing of the transitions decoded by the 4-state models (see Methods). We found that all the six distributions (falls of states 1, 2 and 3; rises of states 2, 3 and 4) significantly deviated from unimodality (Hartigan's Dip test for unimodality, $p < 0.05$). This finding was consistent with the existence of two additional minor states rather than a single fourth 'macro' state. To further investigate these two minor neural states, we then focused our analysis on smaller time windows. Before moving on, please note that we defined as 'micro' states these additional minor neural states that were decoded from only a fraction of the emission sequences and that required narrower ad hoc time windows to be properly studied.

Regarding the first 'micro' state that appeared between DELAY and MOVE, we examined whether it could be related to the 'go' signal event and the preparation of the upcoming movement. Thus, we aligned discharges at this event and trained a 3-state HMM on a temporal window spanning from 250 ms before until 500 ms after. Fig. 4a (cyan color) shows that the probability of this state was lower than the 'macro' states (0.53 and 0.49 at the peak for V6A and PEc, respectively), but it could be still decoded in the majority of sequences (M1: 57 % and 66 %, V6A and PEc respectively; M2: 46 % and 62 %; see Methods). Note that the state probability shown in Fig. 4a is the average of all individual state probability sequences with 3 states which passed the threshold (0.7). Due to the fact that the individual states crossed the threshold at variable time points, the peak of their average could appear globally lowered and below threshold. Moreover, the averaged state sequences were similar across areas and animals ($R^2 > 0.80$; Z-test, $p < 0.05$; see Table S1 for all R^2 values and null distributions). This first 'micro' state emerged 68 ± 154 ms after the 'go' signal and disappeared at 28 ± 102 ms before movement onset in V6A. In comparison, in PEc the corresponding values were 70 ± 152 ms and 34 ± 104 ms (Fig. 4b cyan histograms). After accounting for the variability of the movement onset, the timing uncertainty of this 'micro' state fall was reduced to ± 36−52 ms. These results suggest that a distinct activity pattern was present in both areas during the movement reaction time that we hereafter refer to as PRE-MOVE, thus providing evidence for short-lead movement preparation signals in parietal ensemble activity.

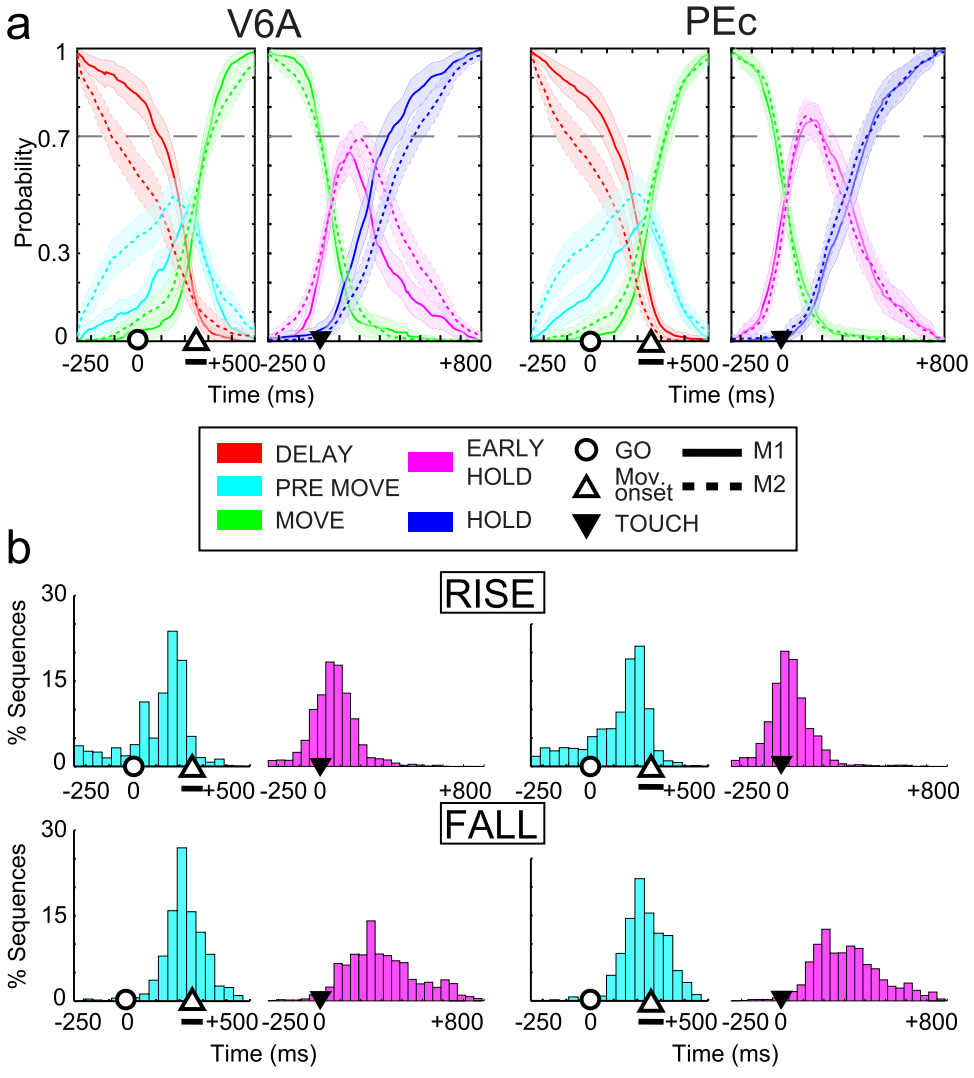

Fig. 4. 'Micro' states revealed by applying HMM in restricted time windows. a) Average state sequences for 3-state HMMs separately trained on two periods, one from 250 ms before to 500 ms after the 'go' signal and the other from 250 before to 800 ms after movement end. Two 'micro' states emerged during movement reaction time and during the first 250 ms after the movement end. Same conventions as in Fig. 2. b) Timing distributions of 'micro' states rises or falls. Same conventions as in Fig. 2.

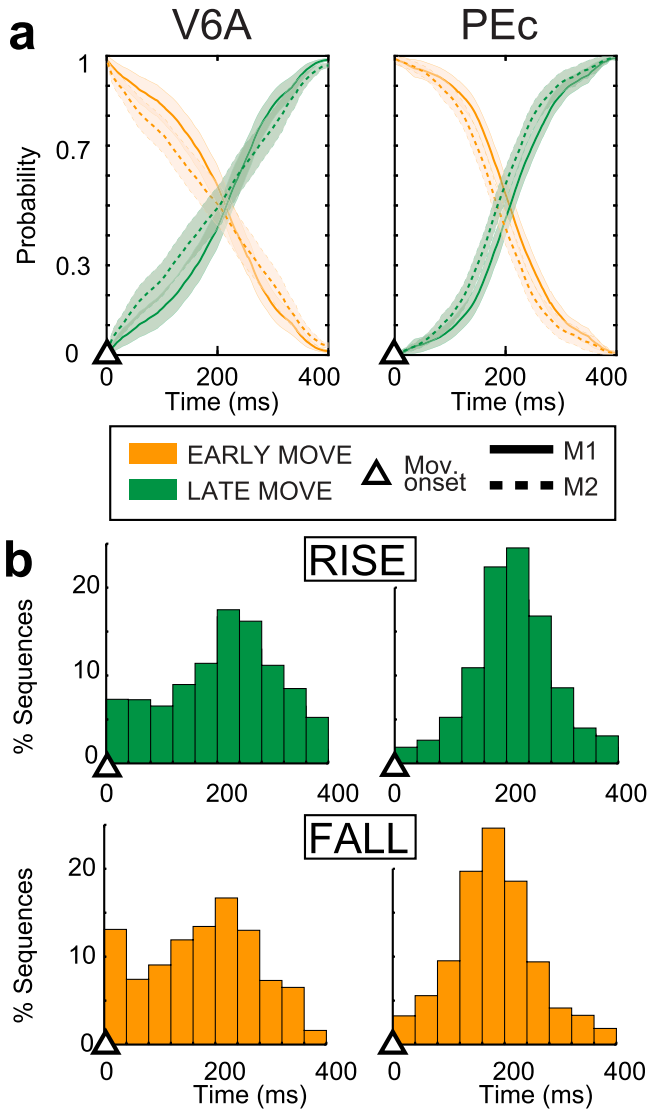

Fig. 5. Segmentation of population activity during movement in two 'micro' states. a) Time course of average state sequences of 2-state HMMs. Activity from movement onset to 400 ms after it were analysed. The transition occurred halfway along the movement. Same conventions as in Fig. 2. b) Timing of state rises or falls. Same conventions as in Fig. 2.

To probe for a 'micro' state also between MOVE and HOLD states, we aligned activity at the movement end event and analyzed a window from 250 ms before until 800 ms after. This window was selected in order to supply the model with enough data to correctly detect possible 'micro' states. Fig. 4a (magenta curves) shows the averaged probability of this state across time, with maximum probability being higher than PRE-MOVE state (0.70 and 0.79, respectively for V6A and PEc) and it was detected in a higher number of sequences (M1: 69 % and 82 %, V6A and PEc respectively; M2: 65 % and 74 %; see Methods). The decoded state sequences were similar across animals and areas ($R^2 > 0.90$; Z-test, $p < 0.05$; see Table S1 for all the values). This 'micro' state rose at 77 ± 131 ms and fell at 314 ± 184 ms after movement end in V6A, while in PEc the corresponding values were 35 ± 109 ms and at 314 ± 166 ms (Fig. 4b magenta histograms). These findings further substantiated the presence of another 'micro' state that was active during the first 250 ms of holding the target period and thus we will refer to it as EARLY HOLD state.

3.4. 'Micro' states during movement were related to distinct movement phases

Lately, it has been reported that HMMs divided the motor cortex activity during arm movement into two states temporally coupled to the two acceleration and deceleration phases of the arm (Kadmon Harpaz et al., 2019). Prompted by this finding, we examined the possibility that a similar movement decomposition could be detected also in parietal cortex ensemble activity. So far single-cell and population parietal activity were reported to encode more spatial movement parameters like direction or trajectory (Mulliken et al., 2008b; Torres et al., 2013). HMMs were trained to search for two states during movement, starting from its onset until 400 ms after, to include the average movement time. Rather unexpectedly for two parietal areas, two states emerged (Fig. 5a) in the vast majority of sequences (M1: 88 % and 80 % in V6A and PEc, respectively; M2: 72 % and 91 %; see Methods) and the decoded state sequence was consistent between animals and areas ($R^2 > 0.90$; Z-test, $p < 0.05$; see Table S1). We refer to these two subsequent 'micro' states as 'EARLY MOVE' and 'LATE MOVE' (see Discussion for further details on their functional meaning).

Even more importantly, the transition between these two states occurred halfway through the analysis window (Fig. 5b) (EARLY MOVE fall: 175 ± 99 and 180 ± 74 ms after movement onset; LATE MOVE rise: 207 ± 99 and 211 ± 72 ms in V6A and PEc, respectively). To examine whether these two states were a model artifact, the R^2 between the real state sequences was compared against a null distribution of synthetic, random state sequences and found to be significantly different (Z-test, $p < 0.05$). This confirmed that the EARLY and LATE MOVE states were not an artifact but reflected real neural processes. In sum, using HMMs, the parietal population activity during the movement was decomposed into two different 'micro' states that very likely reflect the different phases of arm movement (see Discussion).

3.5. Single cell modulations related to 'macro' and 'micro' hidden states

We subsequently tested whether the ensemble activity changes underlying the hidden states and their transitions were present in single neurons. Thus, for each cell, a series of t-tests was performed to compare the firing rate within a fixed window with the firing rates computed in a sliding window of equal duration that moved in 10-ms steps, starting from 1 s before movement onset until 1 s after. At each step the percentage of cells with activity significantly different (*t*-test, $p < 0.05$) between the two windows, was computed. First, we chose as fixed window the time interval that corresponded to the mean duration of MOVE state (from movement onset until 400 ms after). The sliding window spanned from 1000 before movement onset to 1000 after it. As illustrated in Fig. 6a, we observed a significant drop in cell modulations, occurring around the DELAY-MOVE state transition and a sharp increment during MOVE-HOLD switch. Thus, the incidence of single-cell activity modulations matched the three 'macro' states temporal evolution (Fig. 6a). In sum, the majority of neurons (≃ 70 %) changed their firing twice along the trial, thus giving rise to the ensemble activity patterns that were detected by the 3-state HMMs. As a control, we repeated the same procedure taking as reference windows one time interval that included the first 300 ms of delay epoch and another interval at the end (hold epoch) of the temporal window considered for the analyses (see Methods). Fig. S5 shows the results with the two curves superimposed to highlight the abrupt changes in single cell modulations that corresponded to those observed in Fig. 6a. This finding strongly supports that the sharp neural changes were not an artifact, or a bias of

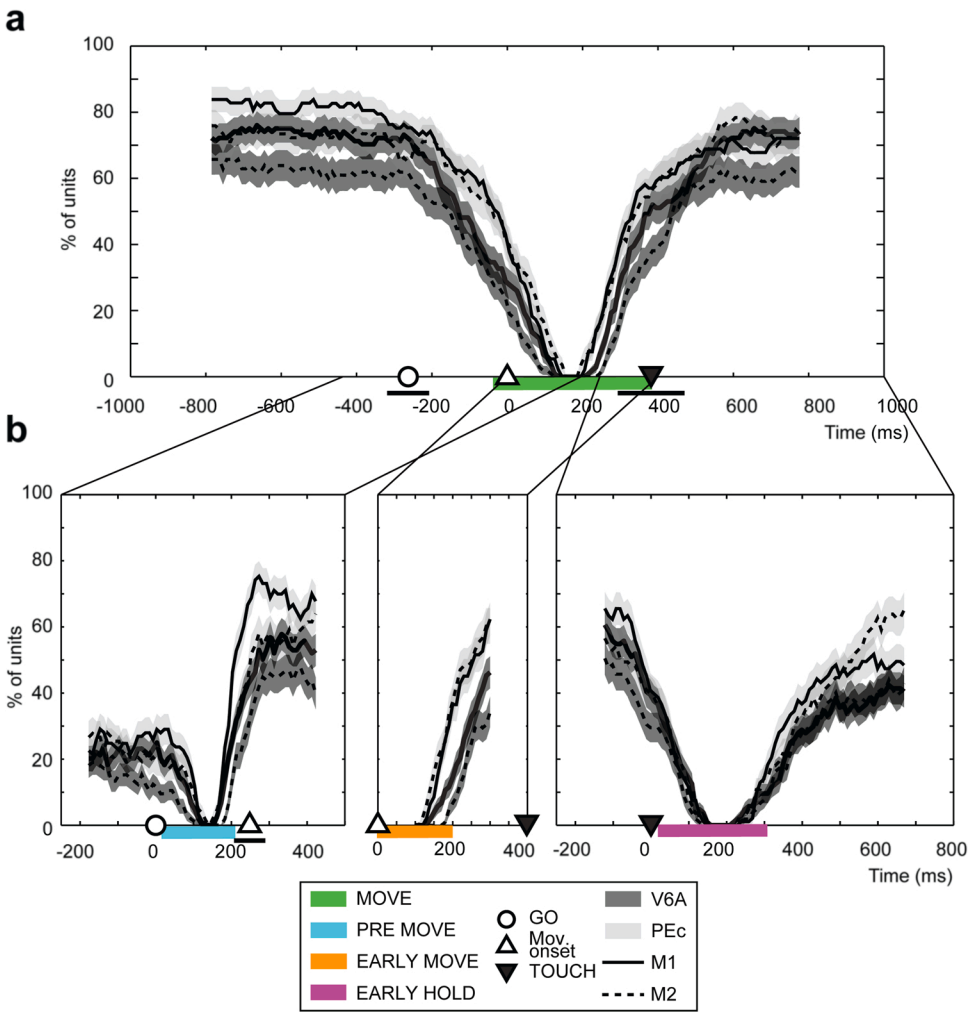

Fig. 6. Single cell modulations underlying population activity neural states. a) Percentage of units with significantly different (*t*-test, $p < 0.05$) firing activity between a fixed window (colored bar below the x-axis corresponding to the mean MOVE neural state) and a sliding window of equal duration (step: 10 ms). Neural data were aligned at movement onset and analyzed from 1000 ms before this event until 1000 after. Shaded areas on the curves illustrate the bootstrap standard deviations. Two sharp change points (−200 to 0 ms and 200 – 400 ms) separate more horizontal segments of the curve and coincide with the transitions between the 3 'macro' neural states b) Percentage of cells with activity changes at the time points around the transitions between the several 'micro' states. Same conventions of Fig. 6a. Curves show steep change points in correspondence with transitions between the different 'micro' neural states.

the analysis used but underlying neural dynamics. To investigate also the relationship of single cell modulations with the several 'micro' states, we performed three additional sliding *t*-test analyses using as fixed windows the PREMOVE, EARLY MOVE and EARLY HOLD states, respectively (Fig. 6b). Accordingly, in each of these analyses the sliding window spanned the same period used to identify the corresponding 'micro' state. Across these tests, we observed that the firing rate of about 25–60 % of the population was significantly different before and after the 'micro' states transitions. In particular, within the movement phase we found that 35–60 % of units significantly changed their firing rates (Fig. 6b middle; see Fig S4 for cell examples). In conclusion, we observed that the 'macro' and 'micro' states of the population activity were linked to single cell modulations.

3.6. *Temporal evolution of population activity within HMM states*

To fully examine the complexity of population dynamics, we performed a principal component analysis (PCA, see Methods) and projected the ensemble activity into a low-dimensional space defined by the first 3 principal components. Fig. 7a shows example neural trajectories of the population activity recorded from V6A (left) and PEc (right) in M1 and M2, respectively (see Fig. S6 for other examples). In both examples, 9 smooth neural trajectories clearly separated from each other were obtained by applying PCA on the condition averaged firing rates (see Methods). Note that the reach goal position was cued before the start of the analysis window, so the trajectories differed between targets from their beginning. In Fig. 7a, on each trajectory the averaged HMM states are indicated with different colours.

It should be noted that the first 3 Principal Components (PCs) accounted for a significant fraction of the variance in the neural data (M1: V6A [21 %+15 %+12 % = 48 %], PEc [25 %+16 %+ 10 % = 51 %]; M2: V6A [16 %+12 %+9% = 37 %]; PEc [22 %+18 %+ 9% = 49 %]).

Interestingly, the EARLY MOVE-LATE MOVE switch occurred at a turning point in population activity halfway between movement onset and target touch, thus confirming a significant change in cells' discharges within the reaching phase (see colours in Fig. 7a and Discussion for more details).

To further confirm quantitatively that each state was associated with a characteristic path of the neural trajectory and to quantify the evolution of neural trajectories, we segmented the trajectories based on the HMM states (Fig. 7b). To this end, we calculated the mean pairwise Euclidean distance between points belonging to segments of the same state (intra-state distance) or different states (inter-state distance). The intra-state distance was significantly lower than the inter-state distance for all the 4 (2 animals x 2 areas) neural populations, indicating that segments (and so, population activity dynamics) were more similar within states than between different states (intra-state distance: 0.17 [0.13 0.19] vs inter-state: 0.41 [0.32 0.52], median [25^{th} 75^{th} quantiles]; Wilcoxon test, $p < 0.001$). In conclusion, despite the strong

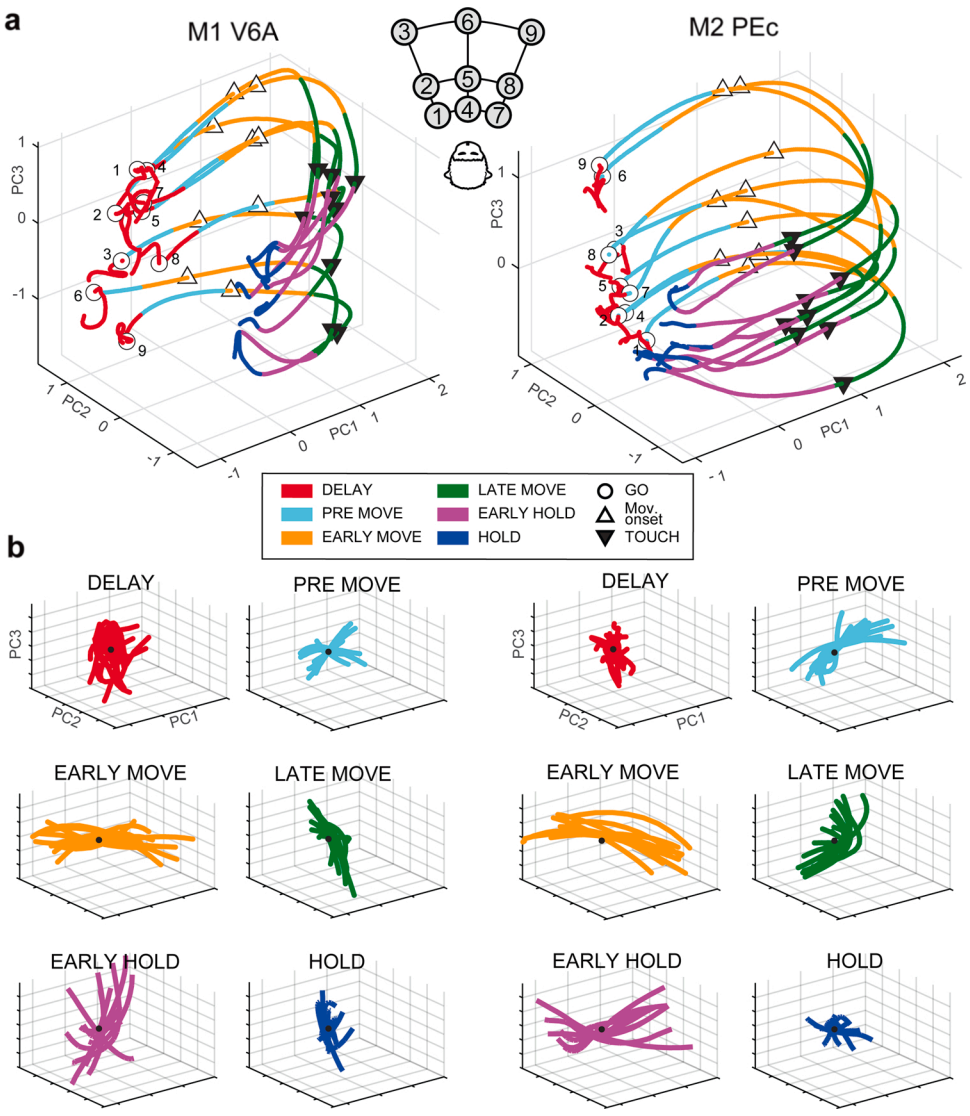

Fig. 7. Neural trajectories and their HMM-based segmentation. a) Neural trajectories averaged across trials relative to each target position (for their precise location, see the schematic legend above) plotted in the 3 first PC's space (left panel: M1 V6A; right: M2 PEc). Different colours correspond to HMM states. Behavioural events: instruction onset (white circle), onset of the movement (white upward triangle) and start of the hold phase (black downward triangle). The population activity for different targets is clearly segregated in the 3D space, but it shows similar evolution in the 9 conditions. The first 3 PCs explained 37–51% of the total variance. b) Segments of neural trajectories cut following the hidden state transitions and with centroids aligned. Same colour code as Fig. 7a). The segments of population activity associated with the neural states show characteristic temporal dynamics that are different from state to state.

assumption on stationarity that is inherent in the HMM method, it still captured the complex neural dynamics of the population activity.

4. Discussion

In the present study we examined the dynamics of the population activity in two medial parietal areas, namely V6A and PEc, well known to contain highly heterogeneous populations that process a variety of spatial and motor features and are active during several phases of the arm reaching task. Using HMMs and PCA analysis, we found these dynamics to be strikingly similar to those reported in motor and premotor cortices, thus highlighting common computational principles during motor control.

4.1. Time course of 'macro' states supports anatomical and functional parieto-frontal gradients

Along the task progress, we observed three main hidden neural states i.e., DELAY, MOVE and HOLD in the two parietal areas ('macro' states). The transition between the DELAY and MOVE states occurred about 60 ms before the movement onset (45 and 75 ms in V6A and PEc, respectively). This transition could reflect a shift from a visuospatial encoding of target location using eye position signals to a somatomotor processing related to the upcoming arm movement. Strong eye position signals have been indeed reported both in V6A and in PEc (Breveglieri et al., 2012; Diomedi et al., 2020; Galletti et al., 1995; Raffi et al., 2008).

The MOVE state rose before the movement onset, probably carrying information about an efferent copy of the motor command sent to PPC to construct a forward model of the movement state (Mulliken et al., 2008a). The most likely source of efferent copy signals is the dorsal premotor cortex (PMd) that sends feedback projections to V6A and PEc (Bakola et al., 2010; Gamberini et al., 2009; Johnson et al., 1996). In this regard, a reaching study in PMd (Kemere et al., 2008) using HMMs reported that the MOVE state emerged about 100 ms before movement onset, thus leading by 55 and 25 ms the MOVE state in V6A and PEc, respectively. This timeline, despite differences in tasks with Kemere et al. (2008), is consistent with an anterior-to-posterior propagation of movement-related signals in the fronto-parietal reaching network. This pattern of information flow has been recently proposed in a revised account of sensorimotor processing in PPC (Medendorp and Heed, 2019).

The transition from MOVE to HOLD state was detected about 40 ms (60 and 15 ms, respectively for V6A and PEc) after the end of movement, thus suggesting that HOLD state encoded somatosensory responses that are known to occur 30−50 ms after stimulation (Cameron et al., 2014; Fromm and Evarts, 1981; Fetz et al., 1980; Soso and Fetz, 1980). The slightly earlier transition to HOLD in PEc compared to V6A could be

attributed to the fact that PEc receives strong somatic inputs directly from PE and area 2 of the somatosensory cortex (Bakola et al., 2010), whereas V6A receives these inputs indirectly from PEc (Gamberini et al., 2009, 2020). Compared to parietal, in frontal cortex (ventral premotor cortex, PMv) the hold state emerged about 95 ms after the movement end (Mazurek et al., 2018). This timing is consistent with the sensory feedback flow from somatosensory to frontal areas via PPC. In sum, the time course of the 'macro' states reported here agrees with previous evidence on PPC organization (Andersen et al., 2014; Buneo and Andersen, 2006; Gamberini et al., 2020; Hadjidimitrakis et al., 2019). At the same time, they support revised views on PPC that extend its role as body state estimator and propose a gradient within PPC that connects a caudal pole which mainly projects body information to the environment to a rostral one performing the opposite function (Medendorp and Heed, 2019). Based on a recent account of the anatomical inputs and functional properties of single neurons in V6A and PEc (Gamberini et al., 2020), it could be argued that these two areas lie just in between these poles.

4.2. 'Micro' states could reflect several sensorimotor processes

In a data driven fashion, we analyzed restricted trial periods to test whether a finer segmentation of population activity was possible. We did find additional 'micro' states that were detected in a variable percentage of the emission sequences and therefore their average probability remained lower than the 'macro' states. Accordingly, the 'micro' states were associated with more transient and weaker cell activation patterns. First, PREMOVE state extended within the movement reaction time (~70 ms after the 'go' signal until 30 ms before movement start). This suggests that PREMOVE reflected a stimulus-driven activity pattern that triggered an internally determined movement preparation period. The 70-ms interval between the 'go' signal and PREMOVE rise is consistent with visual processing latencies in PPC (Kutz et al., 2003; Mulliken et al., 2008a). Although PREMOVE likely reflects sensory processing, processing related also to motor preparation cannot be excluded. A combination of both sensory and motor processing delays in the reaction time activity was reported in PMd (Thura and Cisek, 2014). In PMd, Kemere et al. (2008) reported a transition to a planning HMM state occurring about 100 ms *after* the' go' signal, in line with earlier visual processing in parietal compared to premotor cortex (Cisek and Kalaska, 2010).

Similarly to PREMOVE, the EARLY HOLD followed a behavioral event, emerging slightly after the movement end. It was followed by the HOLD state that included the rest of the holding period. EARLY HOLD could reflect phasic somatosensory discharges related to the initial touch of the target and the subsequent hand stabilization transient phase, whereas HOLD could represent tonic activity required for the maintenance of arm posture. Both phasic and tonic signals related to arm posture have been reported in somatosensory cortex and area PE (Georgopoulos et al., 1984; Hamel-Pâquet et al., 2006; Soso and Fetz, 1980) and they could be relayed to PEc and V6A (Bakola et al., 2010; Gamberini et al., 2020). Another important aspect regards the nature of neural representations during MOVE state. Besides the well-established role in the visuospatial encoding of motor goals (Andersen et al., 2014), parietal cortex is also involved in the arm movement trajectory planning and online control (Archambault et al., 2009; Mulliken et al., 2008b; Torres et al., 2013). From behavioral data, arm movement velocity has been reported to show a roughly bell-shaped profile with peak velocity reached approximately 40–50 % after the movement start (Castiello and Dadda, 2019; Churchland et al., 2006; Roy et al., 2000). Consistent with behavior, our HMM algorithm detected two 'micro' states within the movement period that well corresponded to the acceleration and deceleration phases, respectively, of the arm movement, with their transition occurring half-way through the movement. To our knowledge, a temporal segmentation of population activity like the one observed here has been reported only recently in primary motor cortex where two Markov hidden states coupled to the acceleration and deceleration of the arm were identified (Kadmon Harpaz et al., 2019). Considering that V6A and PEc are caudal PPC areas located far from motor output, this similarity in temporal structure of movement activity is noteworthy. In motor cortex, it was proposed that the two HMM states could originate from the sequential recruitment of two different subpopulations that would drive agonist muscles during acceleration phase and antagonist during deceleration phase (Hoffman and Strick, 1990; Kadmon Harpaz et al., 2019).

An alternative view posits that neural computations and their neural states are shaped by behavioral constraints (Jin et al., 2014; Suway et al., 2018). Indeed, since during reaching there are two main behavioral constraints, i.e. movement start (mostly feedforward) and end (feedback) it is plausible to have two separate states of neural activity. Importantly, the fact that these two states were observed in both parietal and motor cortical areas that lie at different levels in the sensorimotor network, strongly supports this alternative view and suggest that it is a general principle. Accordingly, it is likely that parieto-frontal areas do not control movement in a hierarchical manner but show synchronized intrinsic network dynamics to prepare and generate and execute movements. In this view, even if the dynamics in parietal and frontal areas share the same temporal structure, the information they carry could be qualitatively different due to the heterogeneity of the parietal neurons and the variety of their sensory inputs. In this work, due to the simplicity of the motor task used and the static conditions, we have been able to highlight mainly the temporal similarities between the two nodes of the fronto-parietal network. To unravel more structural and information processing differences, further studies are necessary that will involve more complex tasks with sensory perturbations (e.g. target/-hand perturbations, interceptive movements) and task context information (e.g. serial movements, anti-reaches).

4.3. Single-cell activity modulations and population activity covariance support HMM states

To gain more insight into the underlying mechanisms, we examined the contribution of single neurons in the main HMM states. Gini index analysis revealed that in both parietal areas, the neurons in the population were on average active during two 'macro' states. This clearly demonstrates that the subpopulations that processed each neural state showed an extensive overlap. This finding is in line with previous accounts of V6A and PEc showing that during reach tasks significant numbers of cells were tuned for various spatial and movement parameters at multiple epochs (Diomedi et al., 2020; Hadjidimitrakis et al., 2015, 2017). Despite being active during multiple states, single neurons showed clear modulations of activity in the transitions between both 'macro' and 'micro' states. To evaluate the effect of these single neural behaviors on the ensemble activity, we adopted a population approach different from HMM and explored the population dynamics in continuous neural space using PCA analyses. In particular, recent evidence from motor and premotor cortex suggests that population activity can be represented in the low-dimensional space by a unique neural trajectory with specific dynamics (Afshar et al., 2011; Churchland et al., 2012; Kadmon Harpaz et al., 2019; Petreska et al., 2011).

Similarly, we found here that parietal ensemble activity was represented by smooth trajectories that reflected the spatio-temporal features of the task. Superimposing the neural trajectory of the population activity in the various task conditions with the neural states, we observed that they were not represented by separated points (or small clouds of points), as it would be expected given that stationary firing rate within a state is assumed for Markov processes, but by segments with characteristic paths (Fig. 7). This result further confirmed the HMMs findings and paves the way for a more detailed exploration of parietal neural dynamics during various tasks with state space methods.

Another interesting finding of the neural trajectories' analysis regarded the relative extent of the various states in the neural space. With respect to the states immediately before (PREMOV), during (MOV)

and just after the arm movement (EARLY HOLD), the activity in the initial (DELAY) and final (HOLD) states was much less dynamic. This could be attributed to the fact that our task involved mostly stable sensory processing, with static eye and arm position signals present in DELAY and HOLD states. Overall, it should be acknowledged that our task was somehow biased towards motor-related processing and neural dynamics in parietal cortex should be also studied under more dynamic sensory stimulation (e.g. target/hand perturbation, interceptive movements, bimanual coordination) to study how feedback loops are integrated in population dynamics.

Moreover, since the present study focused only on a restricted part of medial PPC, it remains to be shown whether motor-like neural dynamics are present in other neighbouring areas. In this regard, there is recent evidence that during grasping control the lateral PPC area AIP exhibits neural dynamics very similar to that of area F5 of the ventral part of premotor cortex (Michaels et al., 2018). Future work is needed to describe the motor neural dynamics in other associative and cognitive areas of the parietal cortex. Another limitation of our study is that no recordings of arm kinematics and muscle activity were performed. This information would have helped us to give a better functional characterisation of the microstates, especially those that emerged during movement and hold phase. In particular, EMG and kinematics could help us to understand how the movement phases are related to specific patterns of muscle activities during reaching and during the stabilization of the hand.

In conclusion, the present work highlights important similarities between parietal and motor cortices population activity not reported before. These results support the interpretation of the parietal cortex as a dynamic computational node that is able to cancel out extrinsic inputs and tune its population activity with the premotor and motor cortices to generate movement.

Author contributions

S.D. and F.E.V. were responsible for designing and performing the analysis. S.D., F.E.V. and K.H. interpreted the results. S.D. and F.E.V. wrote the original draft. P.F., C.G. and K.H. assisted in manuscript review, P.F. provided funding and facilities. All authors contributed to editing the manuscript.

Funding

This work was supported by grant H2020-EIC-FETPROACT-2019-951910-MAIA.

Declaration of Competing Interest

The authors declare no competing interests.

Acknowledgments

We thank Drs. Rossella Breveglieri, Annalisa Bosco, Federica Bertozzi, and Giulia Dal Bo' for their help in the recordings; Dr. Lauretta Passarelli, Massimo Verdosci and Francesco Campisi for technical assistance; and Dr. Michela Gamberini for anatomical reconstructions.

Appendix A. The Peer Review Overview and Supplementary data

The Peer Review Overview and Supplementary data associated with this article can be found in the online version, at doi:https://doi.org/10.1016/j.pneurobio.2021.102116.

References

Afshar, A., Santhanam, G., Yu, B.M., Ryu, S.I., Sahani, M., Shenoy, K.V., 2011. Single-trial neural correlates of arm movement preparation. Neuron 71 (3), 555–564. https://doi.org/10.1016/j.neuron.2011.05.047.

Andersen, R.A., Kellis, S., Klaes, C., Aflalo, T., 2014. Toward more versatile and intuitive cortical brain-machine interfaces. Current biology: CB 24 (18), R885–R897. https://doi.org/10.1016/j.cub.2014.07.068.

Archambault, P.S., Caminiti, R., Battaglia-Mayer, A., 2009. Cortical mechanisms for online control of hand movement trajectory: the role of the posterior parietal cortex. Cereb. Cortex 19 (12), 2848–2864. https://doi.org/10.1093/cercor/bhp058.

Bakola, S., Gamberini, M., Passarelli, L., Fattori, P., Galletti, C., 2010. Cortical connections of parietal field PEc in the macaque: linking vision and somatic sensation for the control of limb action. Cereb. Cortex 20 (11), 2592–2604. https://doi.org/10.1093/cercor/bhq007.

Ben Hamed, S., Schieber, M.H., Pouget, A., 2007. Decoding M1 neurons during multiple finger movements. J. Neurophysiol. 98 (1), 327–333. https://doi.org/10.1152/jn.00760.2006.

Bollimunta, A., Totten, D., Ditterich, J., 2012. Neural dynamics of choice: single-trial analysis of decision-related activity in parietal cortex. J. Neurosci. 32 (37), 12684–12701. https://doi.org/10.1523/JNEUROSCI.5752-11.2012.

Breveglieri, R., Hadjidimitrakis, K., Bosco, A., Sabatini, S.P., Galletti, C., Fattori, P., 2012. Eye position encoding in three-dimensional space: integration of version and vergence signals in the medial posterior parietal cortex. J. Neurosci. 32 (1), 159–169. https://doi.org/10.1523/JNEUROSCI.4028-11.2012.

Buneo, C.A., Andersen, R.A., 2006. The posterior parietal cortex: sensorimotor interface for the planning and online control of visually guided movements. Neuropsychologia 44 (13), 2594–2606. https://doi.org/10.1016/j.neuropsychologia.2005.10.011.

Cameron, B.D., de la Malla, C., López-Moliner, J., 2014. The role of differential delays in integrating transient visual and proprioceptive information. Front. Psychol. 5, 50. https://doi.org/10.3389/fpsyg.2014.00050.

Castiello, U., Dadda, M., 2019. A review and consideration on the kinematics of reach-to-grasp movements in macaque monkeys. J. Neurophysiol. 121 (1), 188–204. https://doi.org/10.1152/jn.00598.2018.

Churchland, M.M., Santhanam, G., Shenoy, K.V., 2006. Preparatory activity in premotor and motor cortex reflects the speed of the upcoming reach. J. Neurophysiol. 96 (6), 3130–3146. https://doi.org/10.1152/jn.00307.2006.

Churchland, M.M., Cunningham, J.P., Kaufman, M.T., Foster, J.D., Nuyujukian, P., Ryu, S.I., Shenoy, K.V., 2012. Neural population dynamics during reaching. Nature 487 (7405), 51–56. https://doi.org/10.1038/nature11129.

Cisek, P., Kalaska, J.F., 2010. Neural mechanisms for interacting with a world full of action choices. Annu. Rev. Neurosci. 33, 269–298. https://doi.org/10.1146/annurev.neuro.051508.135409.

Diomedi, S., Vaccari, F.E., Filippini, M., Fattori, P., Galletti, C., 2020. Mixed selectivity in macaque medial parietal cortex during eye-hand reaching. iScience 23 (10), 101616. https://doi.org/10.1016/j.isci.2020.101616.

Fattori, P., Gamberini, M., Kutz, D.F., Galletti, C., 2001. 'Arm-reaching' neurons in the parietal area V6A of the macaque monkey. Eur. J. Neurosci. 13 (12), 2309–2313. https://doi.org/10.1046/j.0953-816x.2001.01618.x.

Fattori, P., Breveglieri, R., Bosco, A., Gamberini, M., Galletti, C., 2017. Vision for prehension in the medial parietal cortex. Cereb. Cortex 27 (2), 1149–1163. https://doi.org/10.1093/cercor/bhv302.

Fetz, E.E., Finocchio, D.V., Baker, M.A., Soso, M.J., 1980. Sensory and motor responses of precentral cortex cells during comparable passive and active joint movements. J. Neurophysiol. 43 (4), 1070–1089. https://doi.org/10.1152/jn.1980.43.4.1070.

Fromm, C., Evarts, E.V., 1981. Relation of size and activity of motor cortex pyramidal tract neurons during skilled movements in the monkey. J. Neurosci. 1 (5), 453–460. https://doi.org/10.1523/JNEUROSCI.01-05-00453.1981.

Gallego, J.A., Perich, M.G., Naufel, S.N., Ethier, C., Solla, S.A., Miller, L.E., 2018. Cortical population activity within a preserved neural manifold underlies multiple motor behaviors. Nat. Commun. 9 (1), 4233. https://doi.org/10.1038/s41467-018-06560-z.

Galletti, C., Battaglini, P.P., Fattori, P., 1995. Eye position influence on the parieto-occipital area PO (V6) of the macaque monkey. Eur. J. Neurosci. 7 (12), 2486–2501. https://doi.org/10.1111/j.1460-9568.1995.tb01047.x.

Galletti, C., Fattori, P., Kutz, D.F., Gamberini, M., 1999. Brain location and visual topography of cortical area V6A in the macaque monkey. Eur. J. Neurosci. 11 (2), 575–582. https://doi.org/10.1046/j.1460-9568.1999.00467.x.

Gamberini, M., Passarelli, L., Fattori, P., Zucchelli, M., Bakola, S., Luppino, G., Galletti, C., 2009. Cortical connections of the visuomotor parietooccipital area V6Ad of the macaque monkey. J. Comp. Neurol. 513 (6), 622–642. https://doi.org/10.1002/cne.21980.

Gamberini, M., Galletti, C., Bosco, A., Breveglieri, R., Fattori, P., 2011. Is the medial posterior parietal area V6A a single functional area? J. Neurosci. 31 (13), 5145–5157. https://doi.org/10.1523/JNEUROSCI.5489-10.2011.

Gamberini, M., Dal Bò, G., Breveglieri, R., Briganti, S., Passarelli, L., Fattori, P., Galletti, C., 2018. Sensory properties of the caudal aspect of the macaque's superior parietal lobule. Brain Struct. Funct. 223 (4), 1863–1879. https://doi.org/10.1007/s00429-017-1593-x.

Gamberini, M., Passarelli, L., Fattori, P., Galletti, C., 2020. Structural connectivity and functional properties of the macaque superior parietal lobule. Brain Struct. Funct. 225 (4), 1349–1367. https://doi.org/10.1007/s00429-019-01976-9.

Gao, P., Ganguli, S., 2015. On simplicity and complexity in the brave new world of large-scale neuroscience. Curr. Opin. Neurobiol. 32, 148–155. https://doi.org/10.1016/j.conb.2015.04.003.

Georgopoulos, A.P., Kalaska, J.F., Caminiti, R., Massey, J.T., 1982. On the relations between the direction of two-dimensional arm movements and cell discharge in primate motor cortex. J. Neurosci. 2 (11), 1527–1537. https://doi.org/10.1523/JNEUROSCI.02-11-01527.1982.

Georgopoulos, A.P., Caminiti, R., Kalaska, J.F., 1984. Static spatial effects in motor cortex and area 5: quantitative relations in a two-dimensional space. Exp. Brain Res. 54 (3), 446–454. https://doi.org/10.1007/BF00235470.

Hadjidimitrakis, K., Bertozzi, F., Breveglieri, R., Bosco, A., Galletti, C., Fattori, P., 2014. Common neural substrate for processing depth and direction signals for reaching in the monkey medial posterior parietal cortex. Cereb. Cortex 24 (6), 1645–1657. https://doi.org/10.1093/cercor/bht021.

Hadjidimitrakis, K., Dal Bo', G., Breveglieri, R., Galletti, C., Fattori, P., 2015. Overlapping representations for reach depth and direction in caudal superior parietal lobule of macaques. J. Neurophysiol. 114 (4), 2340–2352. https://doi.org/10.1152/jn.00486.2015.

Hadjidimitrakis, K., Bertozzi, F., Breveglieri, R., Galletti, C., Fattori, P., 2017. Temporal stability of reference frames in monkey area V6A during a reaching task in 3D space. Brain Struct. Funct. 222 (4), 1959–1970. https://doi.org/10.1007/s00429-016-1319-5.

Hadjidimitrakis, K., Bakola, S., Wong, Y.T., Hagan, M.A., 2019. Mixed spatial and movement representations in the primate posterior parietal cortex. Front. Neural Circuits 13, 15. https://doi.org/10.3389/fncir.2019.00015.

Hamel-Pâquet, C., Sergio, L.E., Kalaska, J.F., 2006. Parietal area 5 activity does not reflect the differential time-course of motor output kinetics during arm-reaching and isometric-force tasks. J. Neurophysiol. 95 (6), 3353–3370. https://doi.org/10.1152/jn.00789.2005.

Hoffman, D.S., Strick, P.L., 1990. Step-tracking movements of the wrist in humans. II. EMG analysis. J. Neurosci. 10 (1), 142–152. https://doi.org/10.1523/JNEUROSCI.10-01-00142.1990.

Janssen, P., Scherberger, H., 2015. Visual guidance in control of grasping. Annu. Rev. Neurosci. 38, 69–86. https://doi.org/10.1146/annurev-neuro-071714-034028.

Jin, X., Tecuapetla, F., Costa, R.M., 2014. Basal ganglia subcircuits distinctively encode the parsing and concatenation of action sequences. Nat. Neurosci. 17 (3), 423–430. https://doi.org/10.1038/nn.3632.

Johnson, P.B., Ferraina, S., Bianchi, L., Caminiti, R., 1996. Cortical networks for visual reaching: physiological and anatomical organization of frontal and parietal lobe arm regions. Cereb. Cortex 6 (2), 102–119. https://doi.org/10.1093/cercor/6.2.102.

Kadmon Harpaz, N., Ungarish, D., Hatsopoulos, N.G., Flash, T., 2019. Movement decomposition in the primary motor cortex. Cereb. Cortex 29 (4), 1619–1633. https://doi.org/10.1093/cercor/bhy060.

Kemere, C., Santhanam, G., Yu, B.M., Afshar, A., Ryu, S.I., Meng, T.H., Shenoy, K.V., 2008. Detecting neural-state transitions using hidden Markov models for motor cortical prostheses. J. Neurophysiol. 100 (4), 2441–2452. https://doi.org/10.1152/jn.00924.2007.

Kutz, D.F., Fattori, P., Gamberini, M., Breveglieri, R., Galletti, C., 2003. Early- and late-responding cells to saccadic eye movements in the cortical area V6A of macaque monkey. Exp. Brain Res. 149 (1), 83–95. https://doi.org/10.1007/s00221-002-1337-9.

Kutz, D.F., Marzocchi, N., Fattori, P., Cavalcanti, S., Galletti, C., 2005. Real-time supervisor system based on trinary logic to control experiments with behaving animals and humans. J. Neurophysiol. 93 (6), 3674–3686. https://doi.org/10.1152/jn.01292.2004.

Luczak, A., McNaughton, B.L., Harris, K.D., 2015. Packet-based communication in the cortex. Nature reviews. Neuroscience 16 (12), 745–755. https://doi.org/10.1038/nrn4026.

Luppino, G., Ben Hamed, S., Gamberini, M., Matelli, M., Galletti, C., 2005. Occipital (V6) and parietal (V6A) areas in the anterior wall of the parieto-occipital sulcus of the macaque: a cytoarchitectonic study. Eur. J. Neurosci. 21 (11), 3056–3076. https://doi.org/10.1111/j.1460-9568.2005.04149.x.

Maboudi, K., Ackermann, E., de Jong, L.W., Pfeiffer, B.E., Foster, D., Diba, K., Kemere, C., 2018. Uncovering temporal structure in hippocampal output patterns. eLife 7, e34467. https://doi.org/10.7554/eLife.34467.

Matelli, M., Govoni, P., Galletti, C., Kutz, D.F., Luppino, G., 1998. Superior area 6 afferents from the superior parietal lobule in the macaque monkey. J. Comp. Neurol. 402 (3), 327–352.

Mazurek, K.A., Schieber, M.H., 2019. Mirror neurons precede non-mirror neurons during action execution. J. Neurophysiol. 122 (6), 2630–2635. https://doi.org/10.1152/jn.00653.2019.

Mazurek, K.A., Rouse, A.G., Schieber, M.H., 2018. Mirror neuron populations represent sequences of behavioral epochs during both execution and observation. J. Neurosci. 38 (18), 4441–4455. https://doi.org/10.1523/JNEUROSCI.3481-17.2018.

Medendorp, W.P., Heed, T., 2019. State estimation in posterior parietal cortex: distinct poles of environmental and bodily states. Prog. Neurobiol. 183, 101691 https://doi.org/10.1016/j.pneurobio.2019.101691.

Michaels, J.A., Dann, B., Scherberger, H., 2016. Neural population dynamics during reaching are better explained by a dynamical system than representational tuning. PLoS Comput. Biol. 12 (11) https://doi.org/10.1371/journal.pcbi.1005175 e1005175.

Michaels, J.A., Dann, B., Intveld, R.W., Scherberger, H., 2018. Neural dynamics of variable grasp-movement preparation in the macaque frontoparietal network. J. Neurosci. 38 (25), 5759–5773. https://doi.org/10.1523/JNEUROSCI.2557-17.2018.

Mulliken, G.H., Musallam, S., Andersen, R.A., 2008a. Forward estimation of movement state in posterior parietal cortex. Proc. Natl. Acad. Sci. U. S. A. 105 (24), 8170–8177. https://doi.org/10.1073/pnas.0802602105.

Mulliken, G.H., Musallam, S., Andersen, R.A., 2008b. Decoding trajectories from posterior parietal cortex ensembles. J. Neurosci. 28 (48), 12913–12926. https://doi.org/10.1523/JNEUROSCI.1463-08.2008.

Omrani, M., Kaufman, M.T., Hatsopoulos, N.G., Cheney, P.D., 2017. Perspectives on classical controversies about the motor cortex. J. Neurophysiol. 118 (3), 1828–1848. https://doi.org/10.1152/jn.00795.2016.

Pandya, D.N., Seltzer, B., 1982. Intrinsic connections and architectonics of posterior parietal cortex in the rhesus monkey. J. Comp. Neurol. 204 (2), 196–210. https://doi.org/10.1002/cne.902040208.

Petreska, B., Yu, B.M., Cunningham, J.P., Santhanam, G., Ryu, S.I., Shenoy, K.V., Sahani, M., 2011. Dynamical segmentation of single trials from population neural data. Adv. Neural Inf. Process. Syst. 24, 756–764 (2011).

Rabiner, L.R., 1989. A tutorial on hidden Markov models and selected applications in speech recognition. Proc. IEEE 77, 257–286. https://doi.org/10.1109/5.18626.

Raffi, M., Ballabeni, A., Maioli, M.G., Squatrito, S., 2008. Neuronal responses in macaque area PEc to saccades and eye position. Neuroscience 156 (3), 413–424. https://doi.org/10.1016/j.neuroscience.2008.08.018.

Roy, A.C., Paulignan, Y., Farnè, A., Jouffrais, C., Boussaoud, D., 2000. Hand kinematics during reaching and grasping in the macaque monkey. Behav. Brain Res. 117 (1-2), 75–82. https://doi.org/10.1016/s0166-4328(00)00284-9.

Sadtler, P.T., Quick, K.M., Golub, M.D., Chase, S.M., Ryu, S.I., Tyler-Kabara, E.C., Yu, B. M., Batista, A.P., 2014. Neural constraints on learning. Nature 512 (7515), 423–426. https://doi.org/10.1038/nature13665.

Scott, S.H., Kalaska, J.F., 1997. Reaching movements with similar hand paths but different arm orientations. I. Activity of individual cells in motor cortex. J. Neurophysiol. 77 (2), 826–852. https://doi.org/10.1152/jn.1997.77.2.826.

Shenoy, K.V., Sahani, M., Churchland, M.M., 2013. Cortical control of arm movements: a dynamical systems perspective. Annu. Rev. Neurosci. 36, 337–359. https://doi.org/10.1146/annurev-neuro-062111-150509.

Soso, M.J., Fetz, E.E., 1980. Responses of identified cells in postcentral cortex of awake monkeys during comparable active and passive joint movements. J. Neurophysiol. 43 (4), 1090–1110. https://doi.org/10.1152/jn.1980.43.4.1090.

Suresh, A.K., Goodman, J.M., Okorokova, E.V., Kaufman, M., Hatsopoulos, N.G., Bensmaia, S.J., 2020. Neural population dynamics in motor cortex are different for reach and grasp. eLife 9, e58848. https://doi.org/10.7554/eLife.58848.

Suway, S.B., Orellana, J., McMorland, A., Fraser, G.W., Liu, Z., Velliste, M., Chase, S.M., Kass, R.E., Schwartz, A.B., 2018. Temporally segmented directionality in the motor cortex. Cereb. Cortex 28 (7), 2326–2339. https://doi.org/10.1093/cercor/bhx133.

Thura, D., Cisek, P., 2014. Deliberation and commitment in the premotor and primary motor cortex during dynamic decision making. Neuron 81 (6), 1401–1416. https://doi.org/10.1016/j.neuron.2014.01.031.

Torres, E.B., Quian Quiroga, R., Cui, H., Buneo, C.A., 2013. Neural correlates of learning and trajectory planning in the posterior parietal cortex. Front. Integr. Neurosci. 7, 39. https://doi.org/10.3389/fnint.2013.00039.

Zhang, C.Y., Aflalo, T., Revechkis, B., Rosario, E.R., Ouellette, D., Pouratian, N., Andersen, R.A., 2017. Partially mixed selectivity in human posterior parietal association cortex. Neuron 95 (3), 697–708. https://doi.org/10.1016/j.neuron.2017.06.040 e4.